# Detrended fluctuation analysis for fractals and multifractals in higher dimensions

Gao-Feng Gu[1,2] and Wei-Xing Zhou[1,2,3,*]
[1]School of Business, East China University of Science and Technology, Shanghai 200237, China
[2]Research Center of Systems Engineering, East China University of Science and Technology, Shanghai 200237, China
[3]School of Science, East China University of Science and Technology, Shanghai 200237, China

(Received 8 August 2006; revised manuscript received 16 October 2006; published 7 December 2006)

One-dimensional detrended fluctuation analysis (DFA) and multifractal detrended fluctuation analysis (MFDFA) are widely used in the scaling analysis of fractal and multifractal time series because they are accurate and easy to implement. In this paper we generalize the one-dimensional DFA and MFDFA to higher-dimensional versions. The generalization works well when tested with synthetic surfaces including fractional Brownian surfaces and multifractal surfaces. The two-dimensional MFDFA is also adopted to analyze two images from nature and experiment, and nice scaling laws are unraveled.

DOI: 10.1103/PhysRevE.74.061104 PACS number(s): 05.40.−a, 05.45.Tp, 87.10.+e

## I. INTRODUCTION

Fractals and multifractals are ubiquitous in natural and social sciences [1]. The most usual records of observable quantities are in the form of time series and their fractal and multifractal properties have been extensively investigated. There are many methods proposed for this purpose [2,3], such as spectral analysis, rescaled range analysis (R/S analysis) [4–9], fluctuation analysis [10], detrended fluctuation analysis (DFA) [11–13], wavelet transform module maxima (WTMM) [14–18], and detrended moving average [19–23], to list a few.

The idea of DFA was invented originally to investigate the long-range dependence in coding and noncoding DNA nucleotide sequences [11]. Then it was generalized to study the multifractal nature hidden in time series, termed multifractal DFA (MFDFA) [13]. Due to the simplicity in implementation, the DFA is now becoming the most important method in the field.

Although the WTMM method seems a little complicated, it is no doubt a very powerful method, especially for high-dimensional objects, such as images and scalar and vector fields of three-dimensional turbulence [24–28]. In contrast, the original DFA method is not designed for such purposes. In a recent paper, a first effort is taken to apply DFA to study the roughness features of texture images [29]. Specifically, the DFA is applied to extract Hurst indices of the one-dimensional sequences at different image orientations and their average scaling exponent is estimated. Unfortunately, this is nevertheless a one-dimensional DFA method.

In this work, we generalize the DFA (and MFDFA as well) method from one to higher dimensions. The generalized methods are tested by synthetic surfaces (fractional Brownian surfaces and multifractal surfaces) with known fractal and multifractal properties. The numerical results are in excellent agreement with the theoretical properties. We then apply these methods to practical examples. We argue that there are tremendous potential applications of the generalized DFA to many objects, such as the roughness of fracture surfaces, landscapes, clouds, three-dimensional temperature fields and concentration fields, and turbulence velocity fields.

The paper is organized as follows. In Sec. II, we represent the algorithm of the two-dimensional detrended fluctuation analysis and the two-dimensional multifractal detrended fluctuation analysis. Section III shows the results of the numerical simulations, which are compared with theoretical properties. Applications to practical examples are illustrated in Sec. IV. We discuss and conclude in Sec. V.

## II. METHOD

### A. Two-dimensional DFA

Being a direct generalization, the higher-dimensional DFA and MFDFA have quite similar procedures to the one-dimensional DFA. We shall focus on two-dimensional space and the generalization to higher dimensions is straightforward. The two-dimensional DFA consists of the following steps.

*Step 1*. Consider a self-similar (or self-affine) surface, which is denoted by a two-dimensional array $X(i,j)$, where $i=1,2,\dots,M$ and $j=1,2,\dots,N$. The surface is partitioned into $M_s \times N_s$ disjoint square segments of the same size $s\times s$, where $M_s=[M/s]$ and $N_s=[N/s]$. Each segment can be denoted by $X_{v,w}$ such that $X_{v,w}(i,j)=X(l_1+i,l_2+j)$ for $1\leqslant i,j \leqslant s$, where $l_1=(v-1)s$ and $l_2=(w-1)s$.

*Step 2*. For each segment $X_{v,w}$ identified by $v$ and $w$, the cumulative sum $u_{v,w}(i,j)$ is calculated as follows:

$$u_{v,w}(i,j)=\sum_{k_1=1}^{i}\sum_{k_2=1}^{j}X_{v,w}(k_1,k_2), \tag{1}$$

where $1\leqslant i,j\leqslant s$. Note that $u_{v,w}$ itself is a surface.

*Step 3*. The trend of the constructed surface $u_{v,w}$ can be determined by fitting it with a prechosen bivariate polynomial function $\tilde{u}$. The simplest function could be a plane. In this work, we shall adopt the following five detrending functions to test the validation of the methods:

$$\tilde{u}_{v,w}(i,j)=ai+bj+c, \tag{2}$$

$$\tilde{u}_{v,w}(i,j)=ai^2+bj^2+c, \tag{3}$$

*Electronic address: wxzhou@moho.ess.ucla.edu

 

$$\widetilde{u}_{v,w}(i,j) = aij + bi + cj + d, \tag{4}$$

$$\widetilde{u}_{v,w}(i,j) = ai^2 + bj^2 + ci + dj + e, \tag{5}$$

$$\widetilde{u}_{v,w}(i,j) = ai^2 + bj^2 + cij + di + ej + f, \tag{6}$$

where $1 \leqslant i,j \leqslant s$ and $a$, $b$, $c$, $d$, $e$, and $f$ are free parameters to be determined. These parameters can be estimated easily through simple matrix operations, derived from the least squares method. We can then obtain the residual matrix

$$\epsilon_{v,w}(i,j) = u_{v,w}(i,j) - \widetilde{u}_{v,w}(i,j). \tag{7}$$

The detrended fluctuation function $F(v,w,s)$ of the segment $X_{v,w}$ is defined via the sample variance of the residual matrix $\epsilon_{v,w}(i,j)$ as follows

$$F^2(v,w,s) = \frac{1}{s^2}\sum_{i=1}^{s}\sum_{j=1}^{s}\epsilon_{v,w}(i,j)^2. \tag{8}$$

Note that the mean of the residual is zero due to the detrending procedure.

*Step 4*. The overall detrended fluctuation is calculated by averaging over all the segments, that is,

$$F^2(s) = \frac{1}{M_sN_s}\sum_{v=1}^{M_s}\sum_{w=1}^{N_s}F^2(v,w,s). \tag{9}$$

*Step 5*. Varying the value of $s$ in the range from $s_{\min} \approx 6$ to $s_{\max} \approx \min(M,N)/4$, we can determine the scaling relation between the detrended fluctuation function $F(s)$ and the size scale $s$, which reads

$$F(s) \sim s^H, \tag{10}$$

where $H$ is the Hurst index of the surface [2,30–32], which can be related to the fractal dimension by $D=3-H$ [1,33]. The choice of $s_{\min} \approx 6$ and $s_{\max} \approx \min(M,N)/4$ is determined empirically to ensure a better scaling relation and at least two partitions in each direction.

Since $N$ and $M$ need not be a multiple of the segment size $s$, two orthogonal trips at the end of the profile may remain. In order to take these ending parts of the surface into consideration, the same partitioning procedure can be repeated starting from the other three corners [30].

### B. Two-dimensional MFDFA

Analogous to the generalization of one-dimensional DFA to one-dimensional MFDFA, the two-dimensional MFDFA can be described similarly, such that the two-dimensional DFA serves as a special case of the two-dimensional MFDFA. The two-dimensional MFDFA follows the same first three steps as in the two-dimensional DFA and has two revised steps.

Divide a self-similar (or self-affine) surface $X(i,j)$ into $M_s \times N_s$ ($M_s=[M/s]$ and $N_s=[N/s]$) disjoint phalanx segments. In each segment $X_{v,w}(i,j)$ compute the cumulative sum $u(i,j,s)$ using Eq. (1). With one of the five regression equations, we can obtain $\widetilde{u}(i,j,s)$ to represent the trend in each segment, then we obtain the fluctuation function $F(v,w,s)$ by Eq. (8).

*Step 4*. The overall detrended fluctuation is calculated by averaging over all the segments, that is,

$$F_q(s) = \left\{\frac{1}{M_sN_s}\sum_{v=1}^{M_s}\sum_{w=1}^{N_s}[F(v,w,s)]^q\right\}^{1/q}, \tag{11}$$

where $q$ can take any real value except for $q=0$. When $q=0$, we have

$$F_0(s) = \exp\left\{\frac{1}{M_sN_s}\sum_{v=1}^{M_s}\sum_{w=1}^{N_s}\ln[F(v,w,s)]\right\}, \tag{12}$$

according to l'Hôpital's rule.

*Step 5*. Varying the value of $s$ in the range from $s_{\min} \approx 6$ to $s_{\max} \approx \min(M,N)/4$, we can determine the scaling relation between the detrended fluctuation function $F_q(s)$ and the size scale $s$, which reads

$$F_q(s) \sim s^{h(q)}. \tag{13}$$

In the standard multifractal formalism based on partition function, the multifractal nature is characterized by the scaling exponents $\tau(q)$, which is a nonlinear function of $q$ [34]. For each $q$, we can obtain the corresponding traditional $\tau(q)$ function through

$$\tau(q) = qh(q) - D_f, \tag{14}$$

where $D_f$ is the fractal dimension of the geometric support of the multifractal measure [13]. One can obtain the generalized dimensions $D_q$ [35–37] and the singularity strength function $\alpha(q)$ and the multifractal spectrum $f(\alpha)$ via Legendre transform [34]. In this work, the numerical and real multifractals have $D_f=2$. For fractional Brownian surfaces with a Hurst index $H$, we have $h(q) \equiv H$.

### C. Some remarks on the generalization

To the best of our knowledge, the first few steps of the one-dimensional DFA and MFDFA in literature are organized in the following order. Construct the cumulative sum of the time series and then partition it into segments of the same scale without overlapping. In this way, a direct generalization to higher-dimensional space should be the following.

*Step I*. Construct the cumulative sum

$$u(i,j) = \sum_{k_1=1}^{i}\sum_{k_2=1}^{j}X(k_1,k_2). \tag{15}$$

*Step II*. Partition $u(i,j)$ into $N_s \times M_s$ disjoint square segments. The ensuing steps are the same as those described in Secs. II A and II B.

One can show that, for the one-dimensional DFA and MFDFA, the residual matrix in a given segment is the same no matter which step is processed first, either the cumulative summation or the partitioning. This means that we have two manners of generalizing to higher-dimensional space, that is, steps 1 and 2 in Sec. II A and steps I and II aforementioned. Our numerical simulations show that both these two kinds of generalization gives the correct Hurst index for fractional Brownian surfaces when adopting two-dimensional DFA.

However, the two-dimensional MFDFA with steps I and II gives the wrong $\tau(q)$ function for two-dimensional multifractals with analytic solutions where the power-law scaling is absent, while the generalization with steps 1 and 2 does a nice job.

The difference of the two generalization methods becomes clear when we compare $u_{v,w}(i,j)$ in Eq. (1) with $u(i,j)$ in Eq. (15). We see that $u_{v,w}(l_1+i,l_2+j)$ is localized to the segment $X_{v,w}$, while $u(l_1+i,l_2+j)$ contains extra information outside the segment when $i<l_1$ and $j<l_2$, which is not constant for different $i$ and $j$ and thus cannot be removed by the detrending procedure. In the following sections, we shall therefore concentrate on the correct generalization expressed in Secs. II A and II B.

After the two-dimensional case has been introduced, the multivariate extension of DFA and MFDFA be deduced similarly. We have tested the three-dimensional MFDFA method using a simulated multifractal field. The three-dimensional multifractal field is constructed by partitioning a cube into eight identical smaller cubes and redistributing the measure to these smaller cubes with multipliers 0.09, 0.1, 0.15, 0.2, 0.06, 0.09, 0.14, and 0.17 (see also Sec. III B for more details on the construction of higher-dimensional multifractals). The curves $F_q(s)$ versus $s$ in log-log plot show sound power-law scaling and the empirical $\tau(q)$ points collapse well on the theoretical $\tau(q)$ function. It follows that the scaling behavior in the simulations is similar qualitatively to the two-dimensional case and no adjustment is necessary.

## III. NUMERICAL SIMULATIONS

### A. Synthetic fractional Brownian surfaces

We test the two-dimensional DFA with synthetic fractional Brownian surfaces. There are many different methods to create fractal surfaces, based on Fourier transform filtering [33,38], midpoint displacement and its variants [1,39,40], circulant embedding of covariance matrix [41–44], periodic embedding and fast Fourier transform [45], top-down hierarchical models [46], and so on. In this paper, we use the MATLAB software FRACLAB 2.03 developed by INRIA to synthesize fractional Brownian surfaces with Hurst index $H$.

In our test, we have investigated fractional Brownian surfaces with different Hurst indices $H$ ranging from 0.05 to 0.95 with an increment of 0.05. The size of the simulated surfaces is $500\times500$. For each $H$, we generated 500 surfaces. Each surface is analyzed by the two-dimensional DFA with the five bivariate functions in Eqs. (2)–(6). The results are shown in Fig. 1. We can see that the estimated Hurst indices $\hat{H}$ are very close to the preset values in general. The deviation of the Hurst index $H$ becomes larger for large values of $H$.

In Fig. 2, we show the log-log plot of the detrended fluctuation $F(s)$ as a function of $s$ for two synthetic fractional Brownian surfaces with $H=0.2$ and 0.8, respectively. There is no doubt that the power-law scaling between $F(s)$ and $s$ is very evident and sound. Hence, the two-dimensional DFA is able to capture well the self-similar nature of the fractional Brownian surfaces and results in precise estimation of the Hurst index.

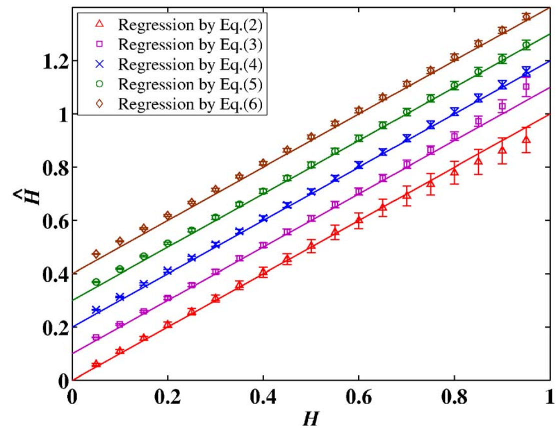


FIG. 1. (Color online) Comparison of the estimated Hurst index $\hat{H}$ using Eqs. (2)–(6) with the true value $H$. The error bars show the standard deviation of the 500 estimated $\hat{H}$ values. The results corresponding to Eqs. (3)–(6) are translated vertically by 0.1, 0.2, 0.3, and 0.4 for clarity.

We also adopted fractional Brownian surfaces to test the two-dimensional multifractal detrended fluctuation analysis. Specifically, we have simulated three fractional Brownian surfaces with Hurst indices $H_1=0.2$, $H_2=0.5$, and $H_3=0.8$, respectively. The five regression equations (2)–(6) are used in the detrending. We calculated $h(q)$ for $q$ ranging from $-10$ to 10 according to Eq. (13). All the $F_q(s)$ functions exhibit excellent power-law scaling with respect to the scale $s$. The function $\tau(q)$ can be determined according to Eq. (14). The resultant $\tau(q)$ functions are plotted in Fig. 3 with the inset showing the $h(q)$ functions. We can find from the figure that, for each surface, the five functions of $\tau(q)$ [and $h(q)$ as well] corresponding to the five detrending functions collapse on a single curve. Moreover, it is evident that $h(q)=H$ and $\tau(q)=qH-2$. The three analytic straight lines intersect at the same point $[q=0,\tau(q)=-2]$. These results are expected according to theoretical analysis.

We stress that, when fractional Brownian surfaces are under investigation, both the two-dimensional DFA and MFDFA can produce the same correct results even when steps I and II are adopted.

### B. Synthetic two-dimensional multifractals

Now we turn to test the MFDFA method with synthetic two-dimensional multifractal measures. There exist several methods for the synthesis of two-dimensional multifractal measures or multifractal rough surfaces [25]. The most classic method follows a multiplicative cascading process, which can be either deterministic or stochastic [47–50]. The simplest one is the $p$ model proposed to mimic the kinetic energy dissipation field in fully developed turbulence [48]. Starting from a square, one partitions it into four subsquares of the same size and chooses randomly two of them to assign the measure of $p/2$ and the remaining two of $(1-p)/2$. This partitioning and redistribution process repeats and we obtain a singular measure $\mu$. A straightforward derivation following

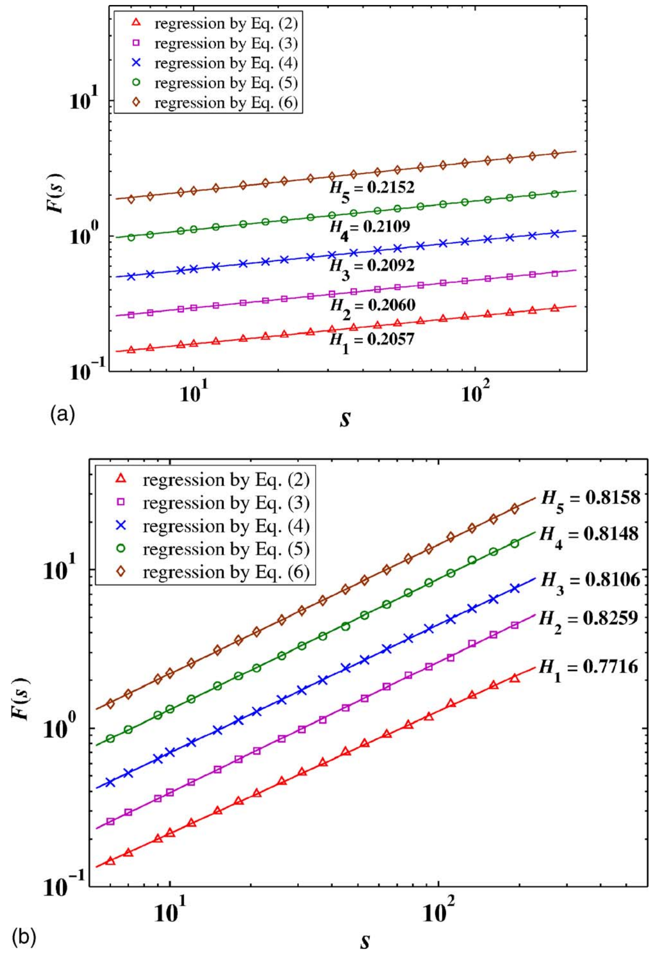


FIG. 2. (Color online) Log-log plots of the detrended fluctuation function $F(s)$ with respect to the scale $s$ for $H=0.2$ (a) and 0.8 (b) using Eqs. (2)–(6). The lines are the least squares fits to the data. The results corresponding to Eqs. (3)–(6) are translated vertically for better presentation.

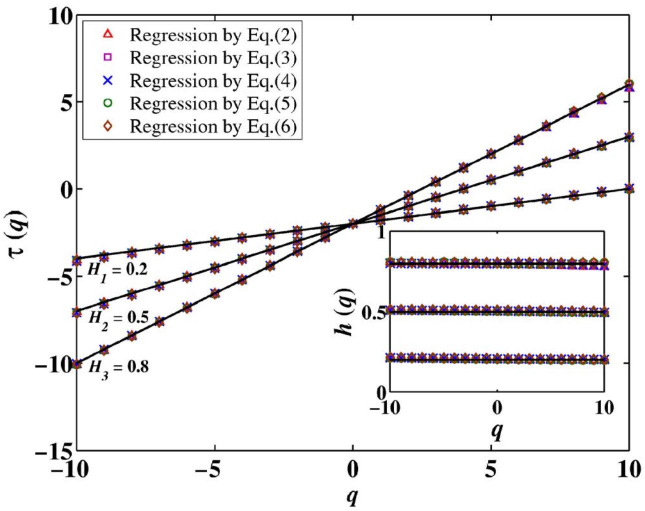


FIG. 3. (Color online) Plots of $\tau(q)$ extracted by using the five detrending functions (2)–(6) as a function of $q$. The three straight lines are $\tau(q)=qH-2$ for $H_1=0.2$, $H_2=0.5$, and $H_3=0.8$, respectively. The inset shows the corresponding $h(q)$ functions.

the partition function method [34] results in the analytic expression

$$\tau(q) = q - 1 - \log_2[p^q + (1-p)^q]. \tag{16}$$

A relevant method is the fractionally integrated singular cascade (FISC) method, which was proposed to model multifractal geophysical fields [51] and turbulent fields [52]. The FISC method consists of a straightforward filtering in Fourier space via fractional integration of a singular multifractal measure generated with some multiplicative cascade process so that the multifractal measure is transformed into a smoother multifractal surface:

$$f(x) = \mu(x) \otimes |x|^{-(1-H)}, \tag{17}$$

where $\otimes$ is the convolution operator and $H \in (0,1)$ is the order of the fractional integration [25], whose $\tau(q)$ function is [25,53]

$$\tau(q) = q(1+H) - 1 - \log_2[p^q + (1-p)^q]. \tag{18}$$

The third one is called the random $\mathcal{W}$ cascade method which generates multifractal rough surfaces from random cascade process on a separable wavelet orthogonal basis [25].

In our test, we adopted the first method for the synthesis of two-dimensional multifractal measure. Starting from a square, one partitions it into four subsquares of the same size and assigns four given proportions of measure $p_1=0.05$, $p_2=0.15$, $p_3=0.20$, and $p_4=0.60$ to them. Then each subsquare is divided into four smaller squares and the measure is redistributed in the same way. This procedure is repeated ten times and we generate multifractal "surfaces" of size $1024 \times 1024$. The resultant $\tau(q)$ functions estimated from the two-dimensional MFDFA method are plotted in Fig. 4, where the inset shows the $h(q)$ functions. We can find that the five functions of $\tau(q)$ [and $h(q)$ as well] corresponding to the five detrending functions collapse on a single curve, which is in excellent agreement with the theoretical formula:

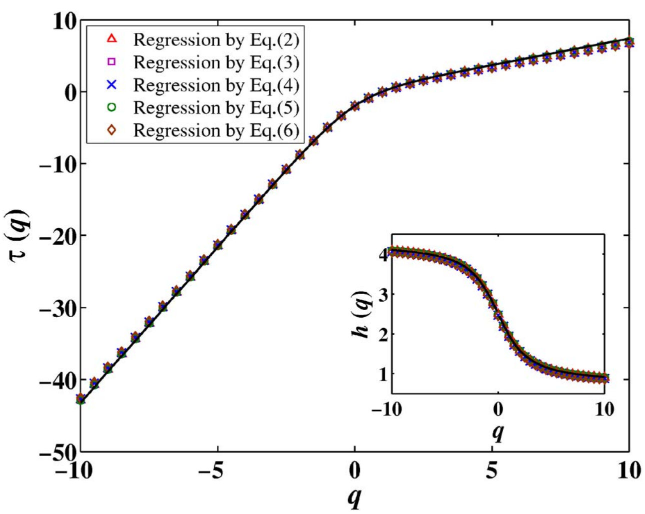


FIG. 4. (Color online) Plots of $\tau(q)$ extracted by using the five detrending functions (2)–(6) as a function of $q$. The continuous line is the theoretical formula (19). The inset shows the corresponding $h(q)$ functions.

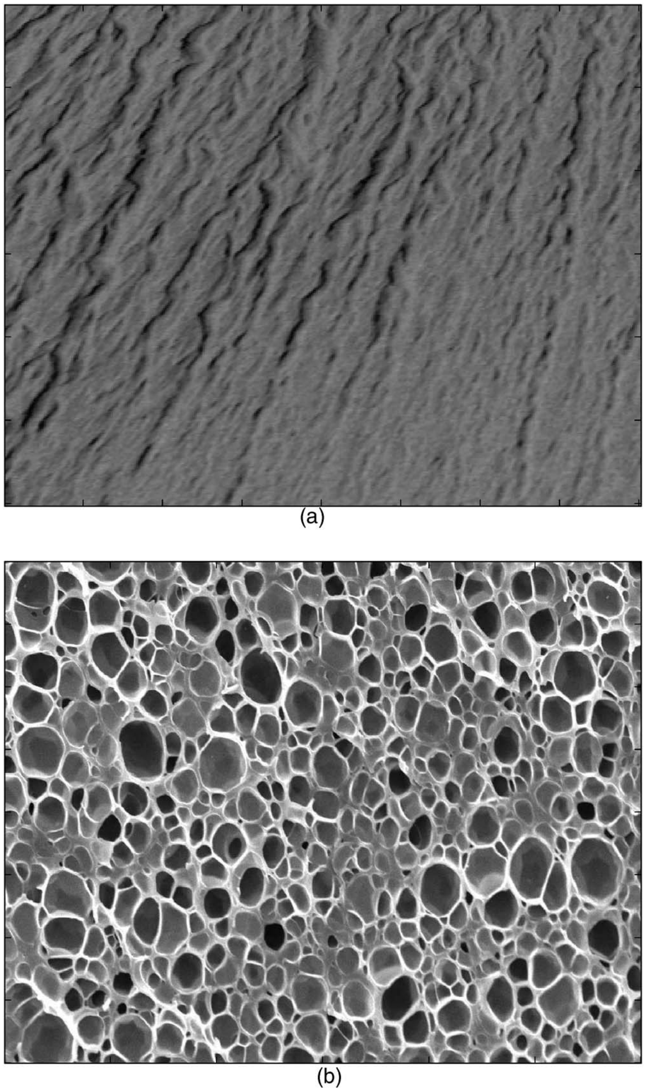

FIG. 5. (a) The image of the Yardangs region on Mars. (b) A scanning electron microscope picture of the surface of a polyurethane sample foamed with supercritical carbon dioxide.

$$\tau(q) = -\log_2(p_1^q + p_2^q + p_3^q + p_4^q). \tag{19}$$

We stress that, when we use steps I and II instead of steps 1 and 2, the resultant $\tau(q)$ estimated by the MFDFA method deviates remarkably from the theoretical formula. Indeed, the power-law scaling for most $q$ values is absent and thus the alternative algorithm with steps I and II and the resulting $\tau(q)$ is completely wrong. In addition, we see that different detrending functions give almost the same results. The linear function (2) is preferred in practice, since it requires the least computational time among the five.

## IV. EXAMPLES OF IMAGE ANALYSIS

### A. The data

In this section we apply the generalized method to analyze two real images, as shown in Fig. 5. Both pictures are investigated by the MFDFA approach since it contains automatically the DFA analysis. The first example is the landscape image of the Mars Yardangs region [29], which can be found at http://sse.jpl.nasa.gov. The size of the landscape image is $2048 \times 1536$ pixels. The second example is a typical scanning electron microscope (SEM) picture of the surface of a polyurethane sample foamed with supercritical carbon dioxide. The size of the foaming surface picture is $1200 \times 800$ pixels.

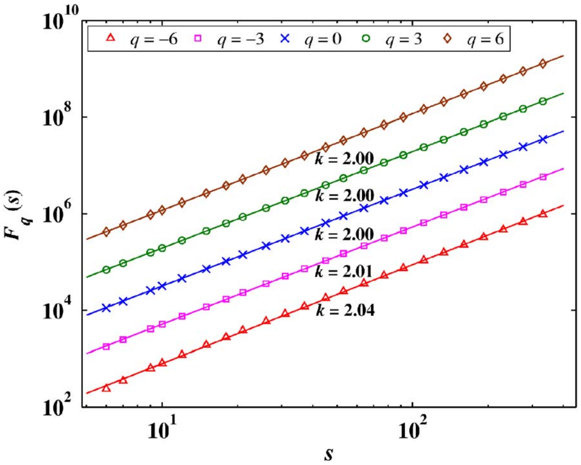


FIG. 6. (Color online) Log-log plots of the detrended fluctuation function $F_q(s)$ versus the lag scale $s$ for five different values of $q$. The continuous lines are the best fits to the data. The plots for $q = -3$, 0, 3, and 6 are shifted upward for clarity.

The SEM picture is of the surface of a polyurethane sample prepared in an experiment of polymer foaming with supercritical carbon dioxide. At the beginning of the experiment, several prepared polyurethane samples were placed in a high-pressure vessel full of supercritical carbon dioxide at saturation temperature for gas sorption. After the samples were saturated with supercritical $CO_2$, the carbon dioxide was quickly released from the high-pressure vessel. Then the foamed polyurethane samples were put into cool water to stabilize the structure cells. Pictures of the foamed samples were taken by a scanning electron microscope.

The two images were stored in the computer as two-dimensional arrays in 256 prey levels. We used Eq. (2) for the detrending procedure. The two-dimensional arrays were investigated by multifractal detrended fluctuation analysis. For each picture, we obtained the $\tau(q)$ function and the $h(q)$ function as well. If $\tau(q)$ is nonlinear with respect to $q$ or, in other words, $h(q)$ is dependent on $q$, then the investigated picture has the nature of multifractality.

### B. Analyzing the Mars landscape image

We first analyze the Mars landscape image shown in the upper panel of Fig. 5 with MFDFA. Figure 6 illustrates the dependence of the detrended fluctuation $F_q(s)$ as a function of the scale $s$ for different values of $q$ marked with different symbols. The continuous curves are the best linear fits. The perfect collapse of the data points on the linear lines indicates the evident power-law scaling between $F_q(s)$ and $s$, which means that the Mars landscape is self-similar.

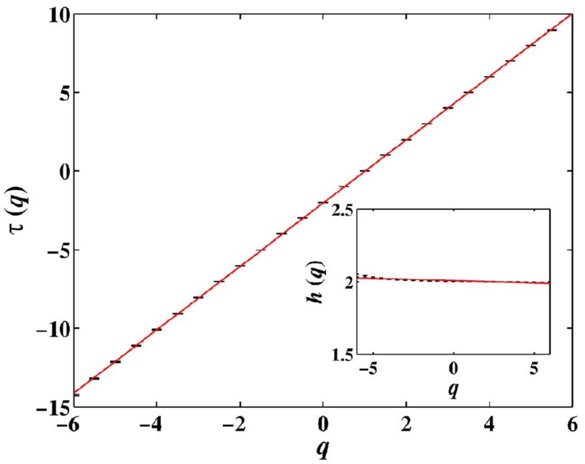


FIG. 7. (Color online) Dependence of $\tau(q)$ with respect to $q$. The solid line is the least squares fit to the data. The inset plots $h(q)$ as a function of $q$.

The slopes of the straight lines in Fig. 6 give the estimates of $h(q)$ and the function $\tau(q)$ can be calculated accordingly. In Fig. 7 is shown the dependence of $\tau(q)$ with respect to $q$ for $-6 \leqslant q \leqslant 6$. We observe that $\tau(q)$ is linear with respect to $q$. The error bars show the standard errors for the regression coefficient estimates [that is, the values of $\tau(q)$] in double-logarithmic coordinates. This excellent linearity of $\tau(q)$ is consistent with the fact that $h(q)$ is almost independent of $q$, as shown in the inset. Hence, the Mars landscape image does not possess multifractal nature.

### C. Analyzing the foaming surface image

Similarly, we analyzed the foaming surface shown in the lower panel of Fig. 5 with the MFDFA method. Figure 8 illustrates the dependence of the detrended fluctuation $F_q(s)$ as a function of the scale $s$ for different values of $q$ marked

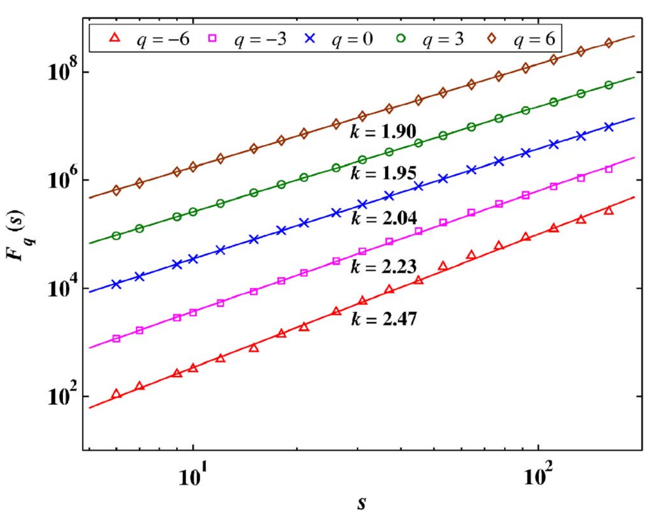


FIG. 8. (Color online) Log-log plots of the detrended fluctuation function $F_q(s)$ versus the lag scale $s$ for five different values of $q$. The continuous lines are the best fits to the data. The plots for $q = -3$, 0, 3, and 6 are shifted upward for clarity.

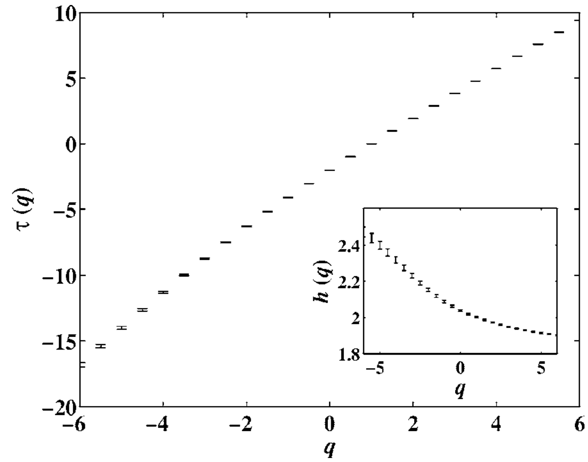


FIG. 9. Dependence of $\tau(q)$ with respect to $q$. The inset shows $h(q)$ as a function of $q$.

with different symbols. The continuous curves are the best linear fits. The perfect collapse of the data points on the linear line indicates the evident power law scaling between $F_q(s)$ and $s$, which means that the Foaming surface is self-similar.

The values of $h(q)$ are estimated by the slopes of the straight lines illustrated in Fig. 8 for different values of $q$. The corresponding function $\tau(q)$ is determined according to Eq. (14). In Fig. 9 is illustrated $\tau(q)$ as a function of $q$ for $-6 \leqslant q \leqslant 6$. The error bars show the standard errors for the regression coefficient estimates. We observe that $\tau(q)$ is nonlinear with respect to $q$, which is further confirmed by the fact that $h(q)$ is dependent of $q$, as shown in the inset. The nonlinearity of $\tau(q)$ and $h(q)$ shows that the foaming surface has multifractal nature.

### D. Sensitivity versus specificity

Another important issue concerns the interpretation of the results of DFA to which less attention has been paid [54]. In the case of one-dimensional R/S analysis, Lo proposes a modified version for the statistical test of long memory and finds that stationary time series with Hurst index larger than 0.5 may stem from short memory [55]. The situation is quite similar in the interpretation of DFA results [54]. In other words, a Hurst index estimated from DFA or R/S analysis that is larger than 0.5 is only a necessary condition for the presence of long memory, but not sufficient. This issue can be discussed in terms of *sensitivity* and *specificity* [54]: A method is sensitive if it is able to identify correctly the property whensoever it is present, while it is specific if, with a high probability, the approach rejects the existence of the property when it is absent. An optimal algorithm would be both sensitive and specific.

In our analysis, we applied techniques to simulated data originating from the class of processes for which the technique has been developed so that we know *a priori* the sensitivity of our method but we do not know its specificity. In other words, we do not exclude the possibility that the scaling behaviors in our analysis of real-world images are generated by other processes. In this sense, we should be cautious in the interpretation of the results. More rigorously speaking, we can state that the two images possess empirically effective self-similarity or empirically effective multifractal nature. In order to test the specificity of the DFA and MFDFA, the numerical simulations should be extended to processes violating the assumptions made by the DFA or MFDFA and investigate the significance level of each process. It is surely impossible to cover all classes of alternative images for the test of specificity. The only realistic way is to adopt self-similarity or multifractality as the null hypothesis and perform statistical tests with respect to an alternative process. Unfortunately, we do not have well-established alternative processes proposed in the literature for the Mars landscape and foaming process. This test should be done when alternative hypotheses are available.

## V. DISCUSSION AND CONCLUSION

In summary, we have generalized the one-dimensional detrended fluctuation analysis and multifractal detrended fluctuation analysis to two-dimensional versions. Further generalization to higher dimensions is straightforward. We have found that the higher-dimensional DFA methods should be performed locally in the sense that the cumulative summation should be conducted after the partitioning of the higher-dimensional multifractal object. Extensive numerical simulations validate our generalization. The two-dimensional MFDFA is applied to the analysis of a Mars landscape image and a foaming surface image. The Mars landscape is found to be a fractal, while the foaming surface exhibits multifractal nature.

It is interesting to consider the possibility of extending other long-range dependence methods to higher dimensions following the idea presented in this work. Indeed, the wavelet transform methods have already been applied to higher-dimensional quantities. We argue that such an extension to higher dimensions is not limited to the DFA and the WTMM method and can be devised for other methods such as R/S analysis, fluctuation analysis, and so on. We have generalized the R/S analysis to two dimensions (2D) and found worse sensitivity compared to the 2D DFA. Moreover, the standard fluctuation analysis is similar to the DFA without the detrending step and the extension to higher dimensions is straightforward. However, a detailed discussion is beyond the scope of the current work.

Finally, we would like to stress that there are tremendous potential applications of the generalized DFA in the analysis of fractals and multifractals. In the two-dimensional case, the methods can be adapted to the investigation of the roughness of fracture surfaces, landscapes, clouds, and many other images possessing self-similar properties. In the case of three dimensions, it could be utilized to qualify the multifractal nature of temperature fields and concentration fields. Possible examples in higher dimensions are strange attractors in nonlinear dynamics. Concrete applications will be reported elsewhere in future presentations.

## ACKNOWLEDGMENTS

The SEM picture was kindly provided by Tao Liu. This work was partially supported by the National Basic Research Program of China (Grant No. 2004CB217703), Fok Ying Tong Education Foundation (Grant No. 101086), and Scientific Research Foundation for the Returned Overseas Chinese Scholars, State Education Ministry of China.

[1] B. B. Mandelbrot, *The Fractal Geometry of Nature* (Freeman, New York, 1983).
[2] M. Taqqu, V. Teverovsky, and W. Willinger, Fractals **3**, 785 (1995).
[3] A. Montanari, M. S. Taqqu, and V. Teverovsky, Math. Comput. Modell. **29**, 217 (1999).
[4] H. E. Hurst, Trans. Am. Soc. Civ. Eng. **116**, 770 (1951).
[5] B. B. Mandelbrot and J. W. Van Ness, SIAM Rev. **10**, 422 (1968).
[6] B. B. Mandelbrot and J. R. Wallis, Water Resour. Res. **5**, 228 (1969).
[7] B. B. Mandelbrot and J. R. Wallis, Water Resour. Res. **5**, 242 (1969).
[8] B. B. Mandelbrot and J. R. Wallis, Water Resour. Res. **5**, 260 (1969).
[9] B. B. Mandelbrot and J. R. Wallis, Water Resour. Res. **5**, 967 (1969).
[10] C.-K. Peng, S. V. Buldyrev, A. L. Goldberger, S. Havlin, F. Sciortino, M. Simons, and H. E. Stanley, Nature (London) **356**, 168 (1992).
[11] C.-K. Peng, S. V. Buldyrev, S. Havlin, M. Simons, H. E. Stanley, and A. L. Goldberger, Phys. Rev. E **49**, 1685 (1994).
[12] K. Hu, P. C. Ivanov, Z. Chen, P. Carpena, and H. E. Stanley, Phys. Rev. E **64**, 011114 (2001).
[13] J. W. Kantelhardt, S. A. Zschiegner, E. Koscielny-Bunde, S. Havlin, A. Bunde, and H. E. Stanley, Physica A **316**, 87 (2002).
[14] M. Holschneider, J. Stat. Phys. **50**, 953 (1988).
[15] J.-F. Muzy, E. Bacry, and A. Arnéodo, Phys. Rev. Lett. **67**, 3515 (1991).
[16] J.-F. Muzy, E. Bacry, and A. Arnéodo, J. Stat. Phys. **70**, 635 (1993).
[17] J.-F. Muzy, E. Bacry, and A. Arnéodo, Phys. Rev. E **47**, 875 (1993).
[18] J.-F. Muzy, E. Bacry, and A. Arnéodo, Int. J. Bifurcation Chaos Appl. Sci. Eng. **4**, 245 (1994).
[19] E. Alessio, A. Carbone, G. Castelli, and V. Frappietro, Eur. Phys. J. B **27**, 197 (2002).
[20] A. Carbone, G. Castelli, and H. E. Stanley, Physica A **344**, 267 (2004).
[21] A. Carbone, G. Castelli, and H. E. Stanley, Phys. Rev. E **69**, 026105 (2004).
[22] J. Alvarez-Ramirez, E. Rodriguez, and J. C. Echeverría, Physica A **354**, 199 (2005).
[23] L. Xu, P. C. Ivanov, K. Hu, Z. Chen, A. Carbone, and H. E. Stanley, Phys. Rev. E **71**, 051101 (2005).

[24] A. Arnéodo, D. Decoster, and S. G. Roux, Eur. Phys. J. B **15**, 567 (2000).
[25] N. Decoster, S. G. Roux, and A. Arnéodo, Eur. Phys. J. B **15**, 739 (2000).
[26] S. G. Roux, A. Arnéodo, and N. Decoster, Eur. Phys. J. B **15**, 765 (2000).
[27] P. Kestener and A. Arneodo, Phys. Rev. Lett. **91**, 194501 (2003).
[28] P. Kestener and A. Arneodo, Phys. Rev. Lett. **93**, 044501 (2004).
[29] J. Alvarez-Ramirez, E. Rodriguez, I. Cervantes, and J. C. Echeverria, Physica A **361**, 677 (2006).
[30] J. W. Kantelhardt, E. Koscielny-Bunde, H. H. A. Rego, S. Havlin, and A. Bunde, Physica A **316**, 441 (2001).
[31] P. Talkner and R. O. Weber, Phys. Rev. E **62**, 150 (2000).
[32] C. Heneghan and G. McDarby, Phys. Rev. E **62**, 6103 (2000).
[33] R. F. Voss, Physica D **38**, 362 (1989).
[34] T. C. Halsey, M. H. Jensen, L. P. Kadanoff, I. Procaccia, and B. I. Shraiman, Phys. Rev. A **33**, 1141 (1986).
[35] P. Grassberger, Phys. Lett. **97A**, 227 (1983).
[36] H. Hentschel and I. Procaccia, Physica D **8**, 435 (1983).
[37] P. Grassberger and I. Procaccia, Physica D **9**, 189 (1983).
[38] *The Science of Fractal Images*, edited by H.-O. Peitgen and D. Saupe (Springer-Verlag, New York, 1988).
[39] A. Fournier, D. Fussell, and L. Carpenter, Commun. ACM **25**, 371 (1982).
[40] E. K. Koh and D. D. Hearn, Comput. Graph. Forum **11**, 169 (1992).
[41] C. R. Dietrich and G. N. Newsam, Water Resour. Res. **29**, 2861 (1993).
[42] C. R. Dietrich and G. N. Newsam, SIAM J. Sci. Comput. (USA) **18**, 1088 (1997).
[43] A. T. A. Wood and G. Chan, J. Comput. Graph. Stat. **3**, 409 (1994).
[44] G. Chan and A. T. A. Wood, J. R. Stat. Soc., Ser. C, Appl. Stat. **46**, 171 (1997).
[45] M. L. Stein, J. Comput. Graph. Stat. **11**, 587 (2002).
[46] A. Penttinen and J. Virtamo, Methodol. Comput. Appl. Probab. **6**, 99 (2004).
[47] B. B. Mandelbrot, J. Fluid Mech. **62**, 331 (1974).
[48] C. Meneveau and K. R. Sreenivasan, Phys. Rev. Lett. **59**, 1424 (1987).
[49] E. A. Novikov, Phys. Fluids A **2**, 814 (1990).
[50] C. Meneveau and K. R. Sreenivasan, J. Fluid Mech. **224**, 429 (1991).
[51] D. Schertzer and S. Lovejoy, J. Geophys. Res. **92**, 9693 (1987).
[52] D. Schertzer, S. Lovejoy, F. Schmitt, Y. Chigirinskaya, and D. Marsan, Fractals **5**, 427 (1997).
[53] J. Arrault, A. Arnéodo, A. Davis, and A. Marshak, Phys. Rev. Lett. **79**, 75 (1997).
[54] D. Maraun, H. W. Rust, and J. Timmer, Nonlinear Processes Geophys. **11**, 495 (2004).
[55] A. W. Lo, Econometrica **59**, 1279 (1991).